

New Inorganic Pigments from Mineral Structures

by
Carlo A. Schettini Mejia

A THESIS

submitted to

Oregon State University

Honors College

in partial fulfillment of
the requirements for the
degree of

Honors Baccalaureate of Science in Chemistry
(Honors Associate)

Presented May 19, 2022
Commencement June 2022

AN ABSTRACT OF THE THESIS OF

Carlo A. Schettini Mejia for the degree of Honors Baccalaureate of Science in Chemistry presented on May 19, 2022. Title: New Inorganic Pigments from Mineral Structures.

Abstract approved: _____
Mas A. Subramanian

The discovery of new blue pigments is a field of great interest, as commercially available pigments present properties that make them undesirable such as poor sustainability, cost, and stability. By researching solid solutions with the melilite structure, we discovered a new solid solution $\text{Sr}_2\text{Zn}_{1-x}\text{Ni}_x\text{Ge}_2\text{O}_7$, with $0.1 \leq x \leq 0.6$, presenting violet coloration that changed systematically through the addition of nickel. The best color was found in $\text{Sr}_2\text{Zn}_{0.4}\text{Ni}_{0.6}\text{Ge}_2\text{O}_7$. The presence of Ni^{2+} was confirmed in the material by using magnetic susceptibility measurements ($x = 0.5$ and 0.6), with the system showing an effective magnetic moment of $4.2 \mu_B$. Measured NIR reflectance was between 30% and 80%, presenting overall better reflectance than cobalt-containing pigments. Therefore $\text{Sr}_2\text{Zn}_{1-x}\text{Ni}_x\text{Ge}_2\text{O}_7$ could be applied as a “cool” pigment. Our Ni-based melilite also has the advantages of better costs and safety than co-based pigments due to the high abundance of nickel. Dielectric measurements performed on the system characterize it as an insulator with nearly temperature and frequency independent dielectric constant and loss tangent.

Keywords: pigments, inorganic chemistry, chemistry, materials.

Corresponding e-mail address: schettic@oregonstate.edu

©Copyright by Carlo A. Schettini Mejia
May 19, 2022

New Inorganic Pigments from Mineral Structures

by
Carlo A. Schettini Mejia

A THESIS

submitted to

Oregon State University

Honors College

in partial fulfillment of
the requirements for the
degree of

Honors Baccalaureate of Science in Chemistry
(Honors Associate)

Presented May 19, 2022
Commencement June 2022

Honors Baccalaureate of Science in Chemistry project of Carlo A. Schettini Mejia presented on May 19, 2022.

APPROVED:

Mas A. Subramanian, Mentor, representing Chemistry

David Ji, Committee Member, representing Chemistry

Jun Li, Committee Member, representing Chemistry

Toni Doolen, Dean, Oregon State University Honors College

I understand that my project will become part of the permanent collection of Oregon State University, Honors College. My signature below authorizes release of my project to any reader upon request.

Carlo A. Schettini Mejia, Author

ACKNOWLEDGEMENTS

In the first place, I would give express my gratitude to my honor's thesis mentor, Dr. Mas Subramanian, who allowed me to collaborate with his research, and guided me through the completion of this project. I want to thank all members of the Subramanian Group who I have had the pleasure of meeting over the years. I would like to thank especially Grace Lin, with whom this project was largely done in collaboration, who was willing to share her experience and help at any step. I would also like to thank Jun Li, whose expertise facilitated the completion of this thesis. Thank you to Dr. Brett Duell, Yu-An Huang, Benjamin Clark, Alyssa Johnson, Dr. Elizabeth Sobalvarro, and others who provided guidance in some way, or I otherwise provided a good environment.

I would like to thank the members of my committee, Dr. Jun Li and Dr. David Ji, who were willing to give their time to review this work. Thank you to Dr. Arthur Ramirez for his collaboration with instrumentation access. Additionally, I would like to thank the OSU instructional faculty for their support throughout the different classes, especially Dr. Chong Fang, Dr. Christine Pastorek, and Dr. Joseph Nibler.

Finally, this would not have been possible without the support of my family and friends. I thank Mario and Claudia Schettini, Cesar Schettini, Brianna Schettini, Rossanna Schettini, Clara and Simon Balid, and Ana Raquel Balid, Claralicia Mejia, Margarita Mejia, for their love and support as a family. I would like to thank my friends, Christopher Bock, Matthew Edwards, Ethan Copple, Maris Amsberry, Justin Perez, Cade Tillema, Fr. John Boyle, Owen Caleen, and the OSU Newman community who made my time at OSU unforgettable.

Chapter 1: Introduction and Background

1.1 Blue Pigments: History and Current Situation

Humans have used pigments since the beginning of history^{1,2}, and these form a ubiquitous component of modern life, present everywhere from clothes to buildings to food. It is therefore important to make sure the commercial pigments present good qualities like durability, cost efficiency, safety, and sustainability. Inorganic pigments are well suited for this function, as, unlike organic pigments, they have intrinsically higher thermal and chemical stability, while being able to match them in other properties.

Historically, blue pigments have been hard to find, and to this day remain the most sought color. The Egyptians and Babylonians used pieces of lapis lazuli, but the process to convert it into the pigment ultramarine was not discovered until the sixth century B.C.¹ Blue in nature is mostly caused by structural phenomena, which make them unsuitable for grinding down into a pigment. Given its rarity as a natural pigment, the Egyptians created the first synthetic blue 5000 years ago when they mixed sand, plant ash, and copper to create Egyptian blue.^{1,2} Since then, the search for synthetic blue pigments has not stopped, and the discovery of new pigments remains a rare and noteworthy event.

This research focused on finding new blue pigments, as it is the rarest color and modern commercial inorganic blues do not present the best qualities. These include synthetic ultramarine ($\text{Na}_7\text{Al}_6\text{Si}_5\text{O}_{24}\text{S}_3$), Prussian blue ($\text{Fe}_4[\text{Fe}(\text{CN})_6]_3$), and spinel cobalt blue (CoAl_2O_4), which suffer from an array of issues including low heat resistance in ultramarine, poor chemical stability in Prussian blue, and toxicity in cobalt blue.^{3,4} Newer pigments like YInMn blue present vibrant colors and useful IR reflectance properties, but

are too expensive for widespread applications.³ The dissatisfaction with the properties of these pigments gives research in this field greater importance than solely aesthetic considerations, as new pigments can offer better sustainability and other useful properties that are not found in common commercial pigments.

1.2 Color Theory: Mechanisms for Color

To understand color in synthesized inorganic pigments, theory presents three main mechanisms that can generate a color. These are *intraatomic excitations (d-d transitions)*, *intervalence charge-transfer excitations*, and *bandgap transitions*.⁵ Although other mechanisms can produce color in minerals and nature, only these three can be easily and consistently replicated in the laboratory and industrial environments to produce new pigments.

Due to interactions from *d*-orbitals with the surrounding ligands, the energy of these orbitals can be split into different levels depending on the geometry of the coordination. Intraatomic excitations occur when photons of specific energies are absorbed to produce a *d-d* excitation, transferring electrons between *d*-orbitals separated by the crystal field energy splitting.⁶ The color observed is complementary to the color absorbed. An example of this can be observed in rubies, where the presence of Cr^{3+} in otherwise colorless corundum (Al_2O_3) gives the compound its iconic red color (Figure. 1.1).

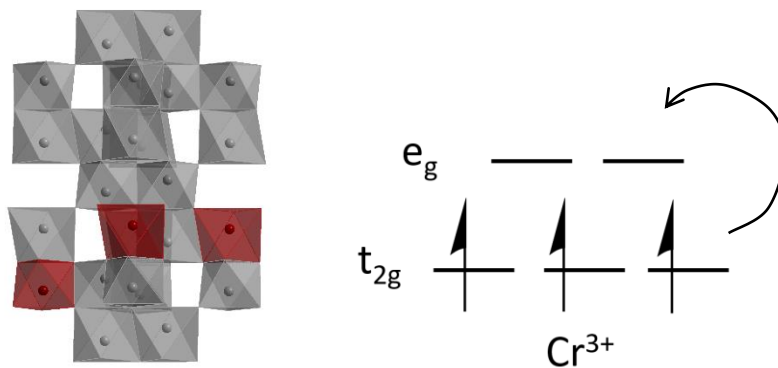


Figure 1.1. Ruby structure with Cr^{3+} atoms marked in red (right), and electronic configuration of Cr^{3+} d -orbitals (left). The electronic transition of electrons from t_{2g} to e_g orbitals causes the coloration of the material.

The occurrence of d - d transitions is ordinarily forbidden due to selection rules, although these can be relaxed, permitting the transitions under special circumstances. The spin selection rule forbids transitions where the spin of the electron has to switch, and the Laporte selection rule indicates that the orbital angular momentum quantum number has to change by $\Delta l = \pm 1$ to conserve angular momentum, as the photon absorbed to produce the transition also contains a unit of angular momentum. Even considering these limitations, d - d transitions remain the most reliable mechanism for generating new pigments.

The second mechanism for color is charge transfers, where color is generated by the absorption of the energy of a photon to transfer an electron between two ions within the lattice, which can be transition metals or ligands.⁶ One classic example of this phenomenon is the coloration of sapphires, which is produced by the transfer of an electron from Fe^{3+} to Ti^{4+} (Figure 1.2). This mechanism typically results in strong coloration when compared to d - d transitions as intraatomic transitions are ‘allowed’ by selection rules.⁶ Similarly to d - d transitions, the color observed is complementary to the color absorbed.

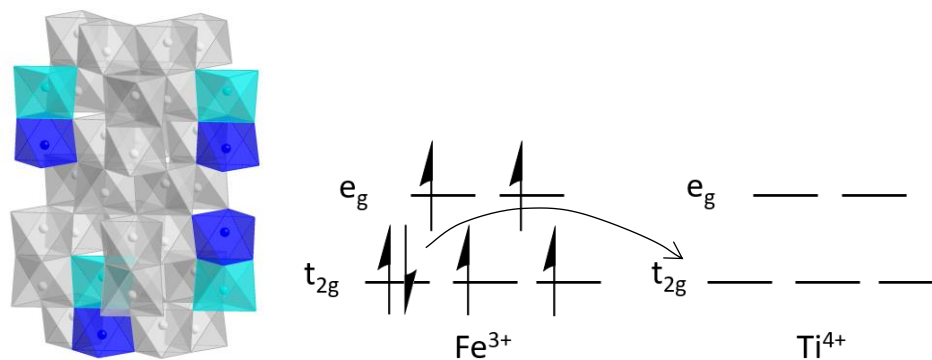


Figure 1.2. Sapphire structure with Fe^{3+} and Ti^{4+} atoms marked in blue and teal (right), and electronic configuration of Fe^{3+} and Ti^{4+} d -orbitals (left). The electronic transition of electrons from iron to titanium orbitals causes the coloration of the material.

The third mechanism is bandgap transitions. In a semiconductor, color can be generated if the bandgap energy is in the visible range of the spectrum, as the material absorbs photons of energy equal to or higher than the bandgap to transfer electrons from the valence band to the conduction band.⁶ Unlike the other two mechanisms, band gaps will not absorb only the light at specific energies but will absorb everything with equal or more energy than the bandgap, so a narrow bandgap would lead to black and not blue.⁶ Therefore, colors obtained from bandgap absorbance do not correspond to the reciprocal color (Figure 1.3) Because of this, bandgap transitions can only be used to generate pigments within the red to yellow range of the spectrum. Some pigments that have this mechanism include vermilion (HgS), and cadmium yellow (CdS), with bandgap energies of 2.0 eV and 2.6 eV respectively.

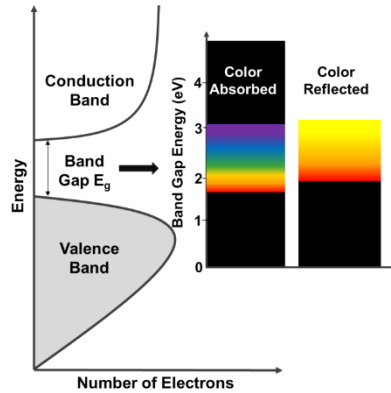


Figure 1.3. Relation between the color absorbed and reflected color in materials with bandgap generated color.

1.3 Magnetic Properties

Diamagnetism occurs when there are no unpaired electrons in the material. When the material is placed inside a magnetic field, it repels it. Materials that have unpaired electrons can present a variety of behaviors when placed in a magnetic field. This is due to the alignment with the field for unpaired electrons within *d* and *f* orbitals of transition metals and lanthanoids in the material.⁷ The different behaviors can be classified as paramagnetic, ferromagnetic, ferrimagnetic, and antiferromagnetic, depending on the alignment of the electron spins with the field (Figure 1.4). The spins of unpaired electrons in paramagnetic materials remain unaligned in the presence of a magnetic field. In ferromagnetic materials, they align parallel to each other, while they align in an antiparallel way for antiferromagnetic materials, canceling any reaction to the field. Ferrimagnetic materials have a mixture of parallel and antiparallel alignments, generating a net moment, although weaker than ferromagnetic materials.

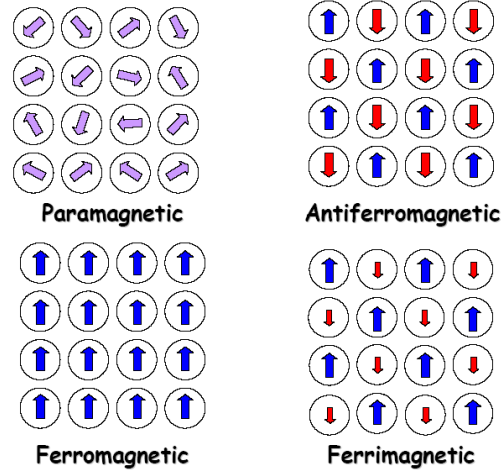


Figure 1.4. Different modes of magnetic ordering of unpaired electrons in the presence of a magnetic field.

To understand the behavior of materials with unpaired electrons, the magnetic susceptibility (χ) for the material was measured at different temperatures. Magnetic susceptibility is a dimensionless constant that indicates how the material responds to the magnetic field. Their behavior can be described using the Curie-Weiss Law (Equation 1), where C is the material-dependent Curie constant, and θ is the Weiss constant.

$$\chi = \frac{C}{T - \theta} \quad (1)$$

By inverting the equation, it is possible to perform a linear regression on the graph of $1/\chi$ vs T to find the Curie constant from Equation 2.

$$\frac{1}{\chi} = \frac{1}{C}(T) - \frac{\theta}{C} \quad (2)$$

Then, the magnetic moment can be calculated from Equations 3-4, where k_B is Boltzmann's constant, and N is the number of magnetic atoms.

$$C = \frac{\mu_0 N}{3k_B} m_{eff}^2 \quad (3)$$

$$\mu_{eff} = 2.84\sqrt{C} \quad (4)$$

It is also possible to predict the magnetic properties of materials using a simple formula (Equations 5-6), where μ_B is the Bohr magneton, n is the number of unpaired electrons, and S is the spin quantum number. This is possible because the spin contributions of electrons occur in a predictable way depending on the number of electrons.

$$\mu_{SO} = \sqrt{n(n + 2)}\mu_B \quad (5)$$

$$\mu_{SO} = \sqrt{4S(S + 1)}\mu_B \quad (6)$$

These calculations can be lower than the measured amounts because they only take into consideration the spin contributions, but not the orbital contributions. Orbitals can contribute to the magnetic moment of the material through rotations. In this case, orbitals that are 90° rotations of each other, that is t_2 orbitals, can rotate and switch places, as long as it does not contradict the Pauli exclusion principle. This is observed more easily in tetrahedrally coordinated transition metals, than octahedrally coordinated ones, as only partially filled t_2 orbitals can contribute to the magnetic moment.

1.4 Dielectric Properties

Dielectric materials are those whose behavior makes them useful for making capacitors, ideally presenting no DC conductivity (Figure 1.5).

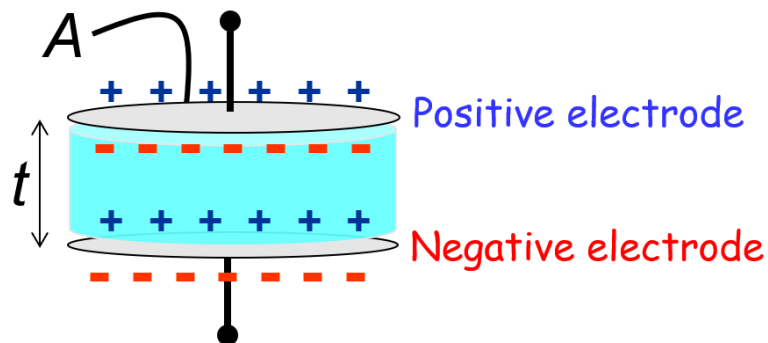


Figure 1.5. Dielectric material (teal) within a capacitor. The area and thickness of the capacitor are denoted by A and t respectively.

One of the main factors that make a material an effective capacitor, is its polarizability. The overall polarizability of the material is composed of the addition of different polarizabilities, which can vary in their contribution at different current frequencies (Figure 1.6). These include electronic, ionic, dipolar, and space charge polarizability.

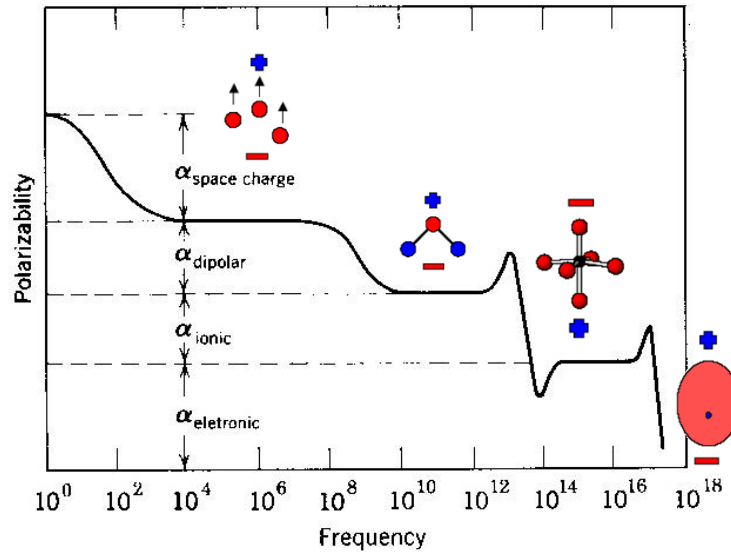


Figure 1.6. Frequency dependence of various polarizabilities.

To characterize the dielectric properties of materials, the dielectric constant and dielectric loss tangent is measured at different temperatures and frequencies. The dielectric constant, also known as relative permittivity, can be determined from the capacitance of the material, as in Equation 7. This value compares the capacitance of the material (C), considering its thickness (t) and area (A), to the permittivity of vacuum (ϵ_0).

$$\epsilon' = \frac{C}{C_0} = \frac{(Ct)}{A\epsilon_0} \quad (7)$$

The dielectric loss tangent ($\tan \delta$) measures how much of the current is lost, with a small dielectric loss indicating a good dielectric. In an ideal dielectric, the current leads

the voltage by 90° , with the phase angle θ and a $\delta = 90 - \theta$, being 90° and 0° respectively (Fig 1.8). Real dielectrics do not follow this behavior perfectly, so some loss is observed.

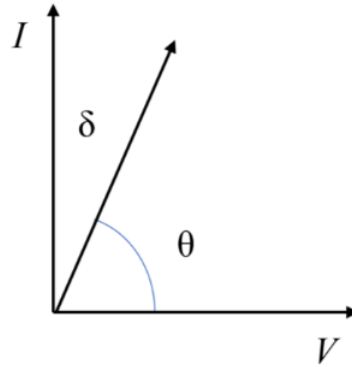


Figure 1.8 Dielectric loss tangent for a dielectric material. Adapted from reference [7].

1.5 Melilite

The crystalline structure chosen for this study was the melilite structure (Figure 1.9). It has the general formula $A_2MM'_2O_7$, where A is a large cation, either an alkaline earth metal or a lanthanide, M and M' are small divalent to hexavalent ions. The structure is a layered tetragonal lattice with lattice parameters $a = b \neq c$, and angles $\alpha = \beta = \gamma = 90^\circ$. M and M' oxides form layers of tetrahedra separated by A layers. Their space group is $P\bar{4}2_1m$.⁸

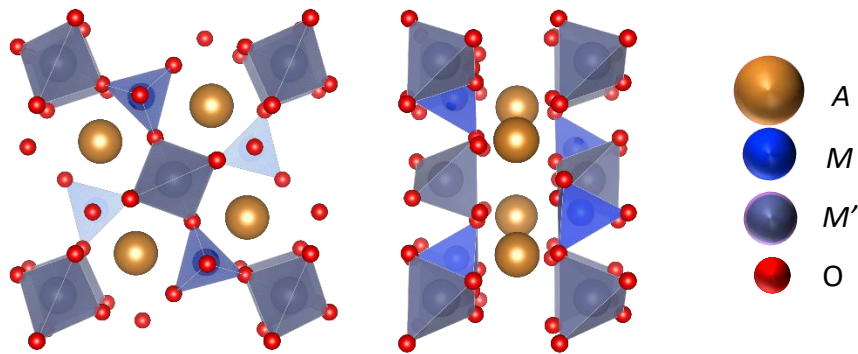


Figure 1.9. View of the melilite structure down the b and c axes.

We chose to study this structure because the tetrahedral layer contains distorted tetrahedra that have the potential for allowing color-generating $d-d$ transitions. Previous

studies in this structure have been able to produce blue pigments using manganese or cobalt as chromophores.⁹ However, these elements are not desirable, as cobalt is carcinogenic and relatively expensive,¹⁰ and manganese present dull colors.¹¹ This study discovered a new solid solution presenting a violet-blue color using nickel as the chromophore.

Chapter 2: Experimental Procedure

Syntheses performed followed the procedures for standard ceramic solid-state reactions. Stoichiometric amounts of metallic oxides and carbonates were ground and mixed in an agate mortar, pressed into pellets, and heated in atmospheric conditions to temperatures between 1200 and 1310 °C for periods of 6 to 12 hours at a time. Samples were reground and reheated multiple times to achieve purity and homogeneity. Powder X-ray diffractometry (XRD) with a Rigaku Miniflex II diffractometer was used to determine purity and unit cell parameters. Internal standards were measured by the addition of NaCl and refined with Le Bail refinements in GSAS EXPGUI software. A Konica Minolta CM-700d spectrophotometer was used to obtain CIE L*a*b* color space coordinates. NIR reflectance and UV-vis measurements were performed using a JASCO V-670 spectrometer up to 2500 nm. Magnetic susceptibility measurements of the $x = 0.5$ and 0.6 samples were taken with a Quantum Design MPMS between 5 K and 300 K. Dielectric constant and loss tangent were measured for all samples between 25 °C and 200 °C.

Chapter 3: Results and discussion

3.1 Structural Analysis

A new solid solution of melilite structure with the formula $\text{Sr}_2\text{Zn}_{1-x}\text{Ni}_x\text{Ge}_2\text{O}_7$ was formed, with x between 0.0 and 0.6, and fitted to the space group symmetry $P\bar{4}2_1m$ (Figure 3.1). Substituting nickel at higher concentrations led to the formation of SrGeO_3 impurities. The solution presented a violet-blue color that became darker through Ni^{2+} substitution.

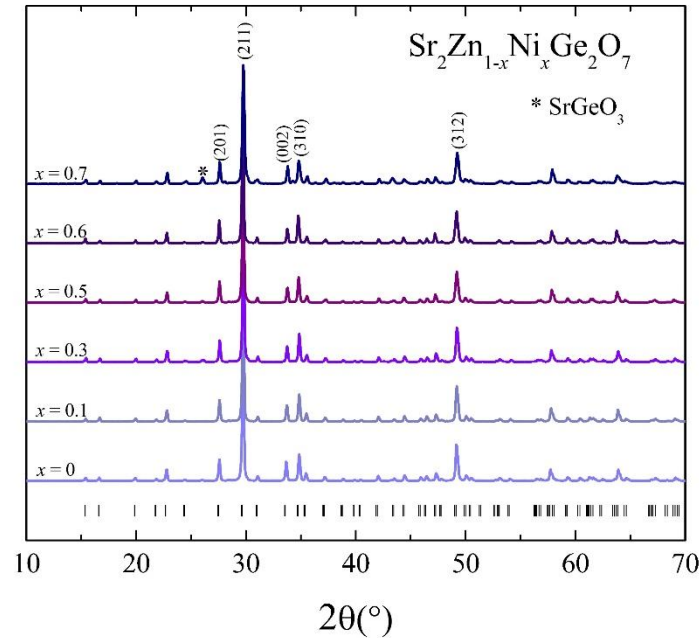


Figure 3.1. XRD patterns for the $\text{Sr}_2\text{Zn}_{1-x}\text{Ni}_x\text{Ge}_2\text{O}_7$ system, with x ranging from 0 to 0.7. At $x = 0.7$, SrGeO_3 impurity peaks start to appear, denoted by asterisks.

Lattice parameter refinements from the XRD indicated an increase in parameter a with the substitution of Ni^{2+} , and a decrease of parameter c (Figure 3.2). Overall, this led to a slight increase in the unit cell volume (Figure 3.2). This is a counterintuitive result, as the ionic radii of Zn^{2+} and Ni^{2+} are 0.6 Å and 0.55 Å respectively.¹² It is likely caused by distortion in the tetrahedral sites and a change in the angle. This will be confirmed by a future neutron diffraction study.

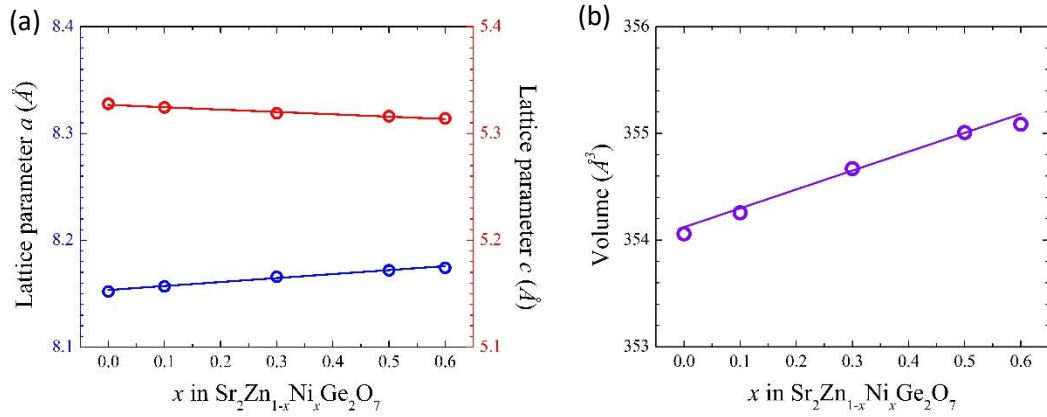


Figure 3.2. (a) Change in lattice parameters a and c with the substitution of Ni^{2+} , and (b) overall change in unit cell size.

3.2 Magnetic Properties

Magnetic susceptibility measurements of samples $x = 0.5$ and 0.6 were taken to study the behavior of the sample and confirm the electronic configuration of nickel (Fig 3.3). Both samples showed paramagnetic behavior between 5 and 300 K. The data were fitted with Equation 2 between 50 and 300 K. The effective magnetic moments, Curie constant, and Weiss constant were calculated for each sample, with diamagnetic corrections (**Table 3.1**).¹³ The measured values were significantly higher than the spin-only theoretical values calculated from Equation 5, but still within the normally observed range for tetrahedral $\text{Ni}^{2+}(d^8)$, that is between 3.7 and $4.47 \mu_B$ (REF). The presence of two unpaired electrons in the t_2 orbitals led to large orbital contributions observed in the difference between the spin-only and experimental values. The negative Weiss constant suggests weak antiferromagnetic interactions.

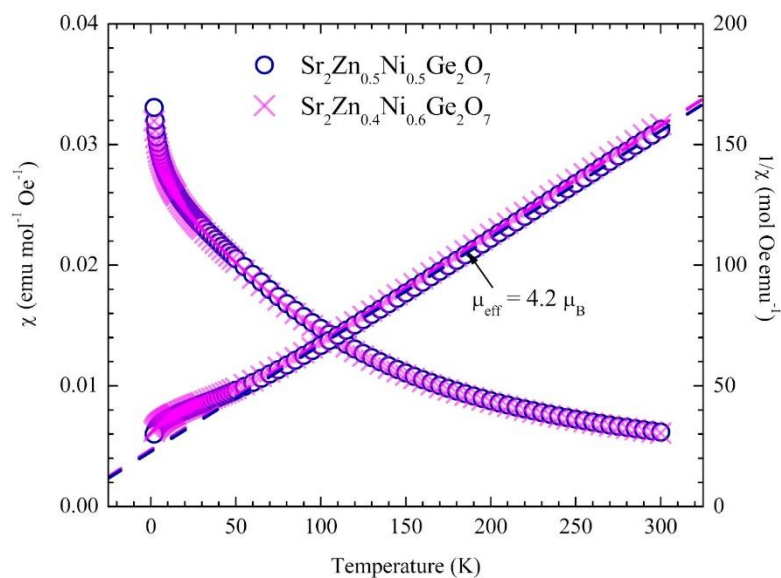


Figure 3.3. Measured magnetic susceptibility and inverse magnetic susceptibility of $\text{Sr}_2\text{Zn}_{0.4}\text{Ni}_{0.6}\text{Ge}_2\text{O}_7$ and $\text{Sr}_2\text{Zn}_{0.5}\text{Ni}_{0.5}\text{Ge}_2\text{O}_7$ between 5 and 300 K.

Table 3.1. Theoretical and calculated magnetic moment, along with observed Curie and Weiss constant for $\text{Sr}_2\text{Zn}_{0.4}\text{Ni}_{0.6}\text{Ge}_2\text{O}_7$ and $\text{Sr}_2\text{Zn}_{0.5}\text{Ni}_{0.5}\text{Ge}_2\text{O}_7$ samples.

Composition	Th. Mag. Moment (μ_B)	Curie Constant	Weiss Constant (K)	Obs. Mag. Moment (μ_B)
$\text{Sr}_2\text{Zn}_{0.5}\text{Ni}_{0.5}\text{Ge}_2\text{O}_7$	2.83	2.26	-51.46	4.2
$\text{Sr}_2\text{Zn}_{0.4}\text{Ni}_{0.6}\text{Ge}_2\text{O}_7$	2.83	2.24	-53.35	4.2

3.3 Optical Properties

The color of $\text{Sr}_2\text{Zn}_{1-x}\text{Ni}_x\text{Ge}_2\text{O}_7$ changed systematically from white to violet through the substitution of Ni^{2+} . (Figure 3.4) The best coloration was observed at $x = 0.6$. The UV-vis absorbance spectra of all pure samples were taken to investigate the origin of the colors (Figure 3.5). From this, the color of the material was determined as originating from the broadening absorption of Ni^{2+} in the tetrahedral site. Previous literature employing this chromophore has also reported blue coloration.¹⁴



Figure 3.4. Color pictures of the synthesized $\text{Sr}_2\text{Zn}_{1-x}\text{Ni}_x\text{Ge}_2\text{O}_7$ solid solution at different x values.

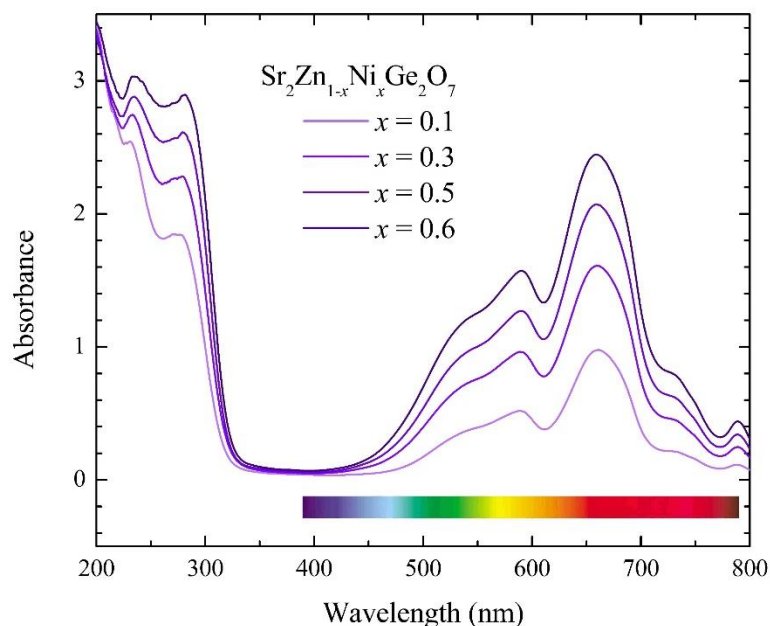


Figure 3.5. Measured UV-vis spectra of $\text{Sr}_2\text{Zn}_{1-x}\text{Ni}_x\text{Ge}_2\text{O}_7$ samples between 200 nm and 800 nm.

In addition, CIE $L^*a^*b^*$ color space measurements were performed to evaluate samples in the $\text{Sr}_2\text{Zn}_{1-x}\text{Ni}_x\text{Ge}_2\text{O}_7$ system and compare them to other pigments (Table 3.2). The CIE $L^*a^*b^*$ system defines colors by three axes, with the L^* axes denoting brightness, a^* going from green to red, and b^* going blue to yellow (Figure 3.6). At $x = 0.5$ and 0.6 , the samples present similar brightness and blue levels, but lower red levels, to those of commercially available cobalt and manganese violets.¹⁵ Based on this, the $\text{Sr}_2\text{Zn}_{1-x}\text{Ni}_x\text{Ge}_2\text{O}_7$ system could be more accurately described as blue-violet or pastel indigo. To our knowledge, the $x = 0.6$ sample presents the highest reported blue character with Ni^{2+} as the sole chromophore. The closest value in literature is -30.38 in

CaLa_{0.5}Al_{11.5}Ni_{0.5}O₁₉. Compared to cobalt blue, the Sr₂Zn_{1-x}Ni_xGe₂O₇ system presents similar brightness but slightly lower blue levels.³ Their application might still be favorable in certain conditions due to other advantages of using nickel as the chromophore.

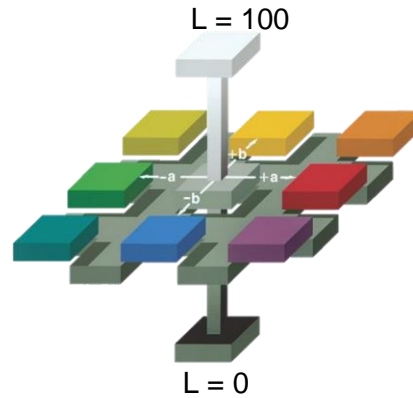


Figure 3.6. Diagram denoting the three axes of the CIE L*a*b* color space.

Table 3.2. L*a*b* coordinates of Sr₂Zn_{1-x}Ni_xGe₂O₇ system, with additional values for common or otherwise relevant pigments for comparison.

Composition	L*	a*	b*
Sr ₂ ZnGe ₂ O ₇	73.66	0.74	3.96
Sr ₂ Zn _{0.9} Ni _{0.1} Ge ₂ O ₇	58.54	1.33	-22.81
Sr ₂ Zn _{0.7} Ni _{0.3} Ge ₂ O ₇	50.98	4.46	-28.84
Sr ₂ Zn _{0.5} Ni _{0.5} Ge ₂ O ₇	45.95	6.42	-32.20
Sr ₂ Zn _{0.4} Ni _{0.6} Ge ₂ O ₇	42.46	8.37	-34.45
Sr ₂ Zn _{0.3} Co _{0.7} Ge ₂ O ₇ (Melilite blue)	34.59	6.52	-45.53
CoAl ₂ O ₄ ^a (Cobalt blue)	43.51	-4.46	-44.39
Co ₃ (PO ₄) ₂ ^b (Cobalt violet)	46	33	-32
YIn _{0.9} Mn _{0.1} O ₃ ^a	40.00	11.90	-47.90
YIn _{0.795} Mn _{0.005} Ti _{0.1} Zn _{0.1} O ₃ ^c	39.36	9.23	-37.15
CaLa _{0.5} Al _{11.5} Ni _{0.5} O ₁₉ ^d	57	-6.5	-30.38

^a From Duell, B. A. et al.³

^b From Kim, S. W. et al.¹⁶

^c From Li, J. et al.¹⁷

^d From Li, J. et al.¹⁴

Near-infrared reflectance spectra for the system were collected and plotted against cobalt-containing pigments (Figure 3.7). It decreased through Ni²⁺ substitution, with the $x = 0.1$ sample presenting values between 30 % and 80% in the 780 nm to 2500 nm range of the electromagnetic spectrum. Compared to the cobalt-bearing pigments, our nickel system presented higher NIR reflectance between 1200 nm and 1600 nm. This indicates that our Ni-based violet would be a better energy-saving material.

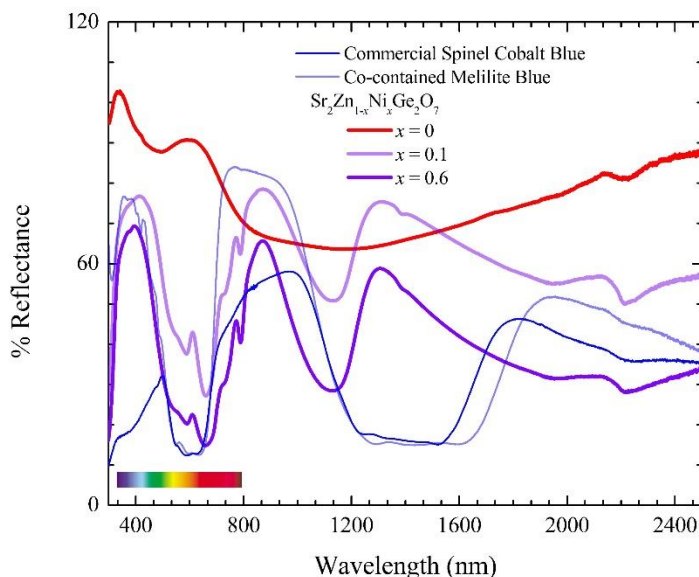


Figure 3.7. Visible and NIR reflectance for selected $\text{Sr}_2\text{Zn}_{1-x}\text{Ni}_x\text{Ge}_2\text{O}_7$ samples, with cobalt-containing pigment spectra for comparison.

3.4 Advantages over Cobalt-containing Pigments

Beyond better NIR reflectance, using nickel as chromophore gives our melilite pigment several significant advantages when compared to commonly used cobalt-containing pigments. The two main ones relate to cost and toxicity. Cobalt is a known carcinogen, while nickel does not present any significant health hazards. The most common adverse effect of nickel exposure is allergic reactions, and it presents no other

known ill effects on human health or ecosystems.¹⁸ Nickel is also significantly less expensive than cobalt due to two times higher natural abundance.¹⁹ Both properties make favorable the development and investment into nickel-containing pigments such as the $\text{Sr}_2\text{Zn}_{1-x}\text{Ni}_x\text{Ge}_2\text{O}_7$ melilite system.

3.5 Dielectric Properties

The dielectric properties of melilite materials have been widely investigated, however, the $\text{Sr}_2\text{Zn}_{1-x}\text{Ni}_x\text{Ge}_2\text{O}_7$ system is new and has not been reported before. The dielectric constant and loss of $\text{Sr}_2\text{Zn}_{0.4}\text{Ni}_{0.6}\text{Ge}_2\text{O}_7$ were measured (Figure 3.8). The dielectric constant presented constant values between 25 °C and 200 °C at all frequencies. Therefore, we concluded the dielectric constant and loss are nearly frequency and temperature independent. The measured constant at 1 MHz and 25 °C was slightly higher than the theoretical values (Table 3.3). The sample can be classified as an insulating material since its dielectric loss is less than 1.

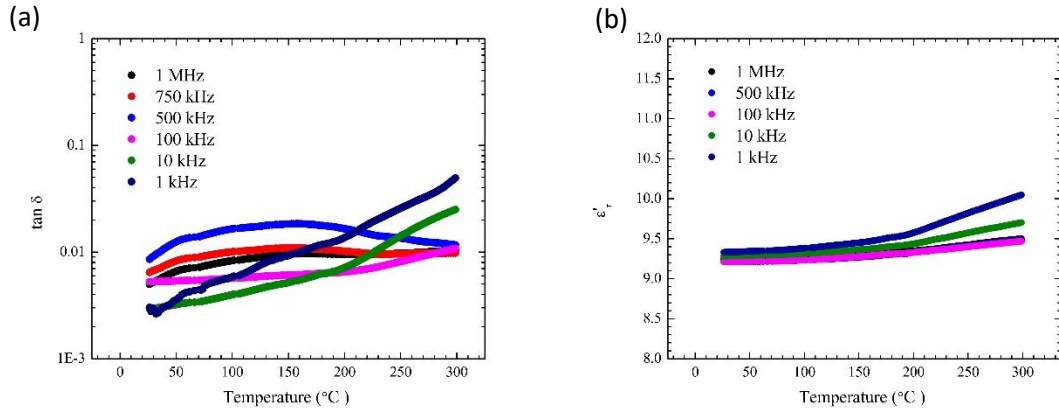


Figure 3.8. Dielectric constant (a) and loss tangent (b) for $\text{Sr}_2\text{Zn}_{1-x}\text{Ni}_x\text{Ge}_2\text{O}_7$ samples at different frequencies and temperatures.

Table 3.3. Measured dielectric constant and loss tangent values at 1 MHz and 25°C.

Composition	Relative Density (%)	Measured ϵ'	Calculated ϵ'	Loss tangent
$\text{Sr}_2\text{Zn}_{0.4}\text{Ni}_{0.6}\text{Ge}_2\text{O}_7$	95	9.25	6.46	0.0016

Chapter 4: Conclusion

In summary, we discovered a new solid solution $\text{Sr}_2\text{Zn}_{1-x}\text{Ni}_x\text{Ge}_2\text{O}_7$, with $0.1 \leq x \leq 0.6$, presenting violet coloration. The best color was found in $\text{Sr}_2\text{Zn}_{0.4}\text{Ni}_{0.6}\text{Ge}_2\text{O}_7$. Through magnetic susceptibility measurements, the presence of Ni^{2+} was determined. Measured NIR reflectance was between 30% and 80%, with the system presenting overall better reflectance than cobalt-containing pigments. When compared with these pigments, our Ni-based melilite also has the advantages of better costs and safety due to the high abundance of nickel. Dielectric measurements performed on the system characterize it as an insulator with nearly temperature and frequency independent dielectric constant and loss tangent.

References

- (1) Kupferschmidt, K. In Search of Blue. *Sci. Mag.* **2019**, *364* (6439), 424–429. <https://doi.org/10.1126/science.364.6439.424>.
- (2) Barnett, J. R.; Miller, S.; Pearce, E. Colour and Art: A Brief History of Pigments. *Opt. Laser Technol.* **2006**, *38* (4), 445–453. <https://doi.org/10.1016/j.optlastec.2005.06.005>.
- (3) Duell, B. A.; Li, J.; Subramanian, M. A. Hibonite Blue: A New Class of Intense Inorganic Blue Colorants. *ACS Omega* **2019**, *4* (26), 22114–22118. <https://doi.org/10.1021/acsomega.9b03255>.
- (4) Li, J.; Subramanian, M. A. Inorganic Pigments with Transition Metal Chromophores at Trigonal Bipyramidal Coordination: Y(In,Mn)O₃ Blues and Beyond. *J. Solid State Chem.* **2019**, *272*, 9–20. <https://doi.org/10.1016/j.jssc.2019.01.019>.
- (5) Nassau, K. Color in Minerals. *Am. Mineral.* **1978**, *63*, 219–229.
- (6) Nassau, K. The Physics and Chemistry of Color: The 15 Mechanisms. In *The Physics and Chemistry of Color*; Elsevier, 2003; pp 247–280.
- (7) Giampaoli, G. Tuning Functional Properties of Pyrochlore and Related Oxides via Cation and Anion Substitutions, Oregon State University, 2018.
- (8) Endo, T.; Doi, Y.; Hinatsu, Y.; Ohoyama, K. Magnetic and Neutron Diffraction Study on Melilite-Type Oxides Sr₂MGe₂O₇ (M = Mn, Co). *Inorg. Chem.* **2012**, *51* (6), 3572–3578. <https://doi.org/10.1021/ic202386h>.
- (9) Dondi, M.; Zanelli, C.; Ardit, M.; Cruciani, G. Co-Doped Hardystonite, Ca₂(Zn,Co)Si₂O₇, a New Blue Ceramic Pigment. *J. Am. Ceram. Soc.* **2011**, *94* (4), 1025–1030. <https://doi.org/10.1111/j.1551-2916.2010.04203.x>.
- (10) Rousseau, M.-C.; Straif, K.; Siemiatycki, J. IARC Carcinogen Update. *Environ. Health Perspect.* **2005**, *113* (9), A580–A581. <https://doi.org/10.1289/ehp.113-1280416>.
- (11) Gramm, G.; Fuhrmann, G.; Ploner, K.; Penner, S.; Huppertz, H. Synthesis of Non-Toxic Inorganic Blue Pigments in the Melilite-Type Structure. *Mater. Adv.* **2020**, *1* (7), 2293–2299. <https://doi.org/10.1039/D0MA00541J>.
- (12) Shannon, R. D. Revised Effective Ionic Radii and Systematic Studies of Interatomic Distances in Halides and Chalcogenides. *Acta Crystallogr. Sect. A* **1976**, *32* (5), 751–767. <https://doi.org/10.1107/S0567739476001551>.
- (13) Bain, G. A.; Berry, J. F. Diamagnetic Corrections and Pascal's Constants. *J. Chem. Educ.* **2008**, *85* (4), 532. <https://doi.org/10.1021/ed085p532>.
- (14) Li, J.; Medina, E. A.; Stalick, J. K.; Sleight, A. W.; Subramanian, M. A. Colored Oxides with Hibonite Structure: A Potential Route to Non-Cobalt Blue Pigments. *Prog.*

Solid State Chem. **2016**, *44* (4), 107–122.

<https://doi.org/10.1016/j.progsolidstchem.2016.11.001>.

(15) Gorodylova, N.; Kosinová, V.; Dohnalová, Ž.; Bělina, P.; Šulcová, P. New Purple-Blue Ceramic Pigments Based on $\text{CoZr}_4(\text{PO}_4)_6$. *Dyes Pigments* **2013**, *98* (3), 393–404. <https://doi.org/10.1016/j.dyepig.2013.03.004>.

(16) Kim, S. W.; Saito, Y.; Hasegawa, T.; Toda, K.; Uematsu, K.; Sato, M. Development of a Novel Nontoxic Vivid Violet Inorganic Pigment – Mn^{3+} -Doped $\text{LaAlGe}_2\text{O}_7$. *Dyes Pigments* **2017**, *136*, 243–247. <https://doi.org/10.1016/j.dyepig.2016.08.038>.

(17) Li, J.; Lorget, S.; Stalick, J. K.; Sleight, A. W.; Subramanian, M. A. From Serendipity to Rational Design: Tuning the Blue Trigonal Bipyramidal Mn^{3+} Chromophore to Violet and Purple through Application of Chemical Pressure. *Inorg. Chem.* **2016**, *55* (19), 9798–9804. <https://doi.org/10.1021/acs.inorgchem.6b01639>.

(18) *The Facts on Nickel | Dartmouth Toxic Metals*. <https://sites.dartmouth.edu/toxmetal/more-metals/nickel-hidden-in-plain-sight/the-facts-on-nickel/> (accessed 2022-04-27).

(19) Su, B.; Cao, Z.-C.; Shi, Z.-J. Exploration of Earth-Abundant Transition Metals (Fe, Co, and Ni) as Catalysts in Unreactive Chemical Bond Activations. *Acc. Chem. Res.* **2015**, *48* (3), 886–896. <https://doi.org/10.1021/ar500345f>.

